Chapter 2

Metal Ions Implantation-Induced Effects in GaN Thin Films

Ghulam Husnain and Morgan Madhuku

Additional information is available at the end of the chapter

http://dx.doi.org/10.5772/68042

Abstract

MOCVD-grown GaN n-type epilayers were implanted with 150keV Co^+ and Cr^+ ions at different fluences at room temperature. Co^+ was implanted at $3x10^{16}$ and 5×10^{16} ions/cm^2 and samples rapid-thermal-annealed at 700, 800 and 900°C for 5 minutes, while Cr^+ was implanted at $3x10^{16}$ ions/cm^2 and annealed at 800 and 900°C for 2 minutes. Diffraction patterns of implanted samples showed satellite peaks at the lower side of the main GaN (0002) reflection and these were assigned to implantation induced-damage and the formation of $Ga_{1-x}Co_xN$ or $Ga_{1-x}Cr_xN$ phases. The coercivity (H_c) at 5K from SQUID for Co^+ implanted GaN at $3x10^{16}$ ions/cm^2 was 275 Oe and that at $5x10^{16}$ ions/cm^2 was 600 Oe. For Cr^+ implanted GaN at $3x10^{16}$ ions/cm^2, Hc was 175 Oe. At the same dose of Cr^+ and Co^+ implanted ions, the saturation magnetization (*Ms*) values were almost similar. But after annealing at 900°C, the *Ms* value of Cr^+ implanted GaN was higher than that of Co^+ implanted at 5K. For Co^+ implanted GaN, magnetization was retained up to 370K while in Cr^+ implanted GaN, magnetization was retained above 380K. These findings are the highest reported Curie temperatures for Co^+ and Cr^+ implanted GaN diluted magnetic semiconductors.

Keywords: GaN, quaternary alloys, microstructure, ion implantation, dilute magnetic semiconductors

1. Introduction

III-Nitrides are currently finding applications in conventional devices, such as UV-Vis laser diodes, ultra-bright LEDs, UV detectors, high temperature electronics, high-density optical data storage, aerospace and automobiles technologies [1]. Furthermore,

III-nitrides, when doped with magnetic impurities, have plentiful possibilities of being used in diluted magnetic semiconductors (DMSs) for spintronic device applications. Most of the above-mentioned devices require well-organized, controlled and targeted area doping. Even though materials can be doped during growth, ion implantation presents various advantages, which are not achievable by doping during growth in III–V nitrides. The low solubility of transition metals in III–V nitrides ($<10^{18}cm^{-3}$) has restricted their doping to produce a range of magnetic semiconducting materials. Major changes in magnetic properties of these materials are not expected because of limit in solubility since there is a direct relationship between magnetic effects and concentration of magnetic impurities.

Ion implantation has a number of advantages [2], some of which are that any dopant atom can be introduced at any desired depth and concentration above solid solubility limit in a material and that doping can be done on a precisely defined area [3]. Moreover, ion implantation offers other advantages such as electrical isolation, dry etching, quantum well intermixing and ion cut [4]. However, ion implantation has its own drawbacks such as lattice damage and generation of new defects [5]. An entrenched solution to get rid of implantation-induced damage is thermal annealing. Moreover, dopants can be optically, electrically and magnetically activated through thermal annealing. However, annealing conditions (time, temperature and atmosphere), sample thickness, cap layers and implantation parameters have to be considered to successfully optimize thermal annealing to recover the lattice.

Considerable progress has been made in micro-electronics since the time discrete circuit elements were replaced by integrated circuits. Scientists have shown keen interest to harness the spin of electrons so as to further improve the functionality of devices [6]. Currently, charge-flow is used to carry information between microelectronic devices; however, spin movement can also be employed to carry information [7]. This has provided prospects of utilizing charge and spin degrees of freedom concurrently to bring about a new generation of electronic devices known as spin-electronics or spintronics. Spintronics is a multidisciplinary field covering physics, chemistry and engineering in which electronic, opto-electronic and magneto-electronic features can be integrated on a single chip [8]. The search for new spintronics materials as well as ways to improve existing materials is still on-going. Diluted magnetic semiconductors (DMSs), which are a class of materials in which a small quantity of magnetic ions is introduced into normal semiconductors, have been found to be suitable for spintronic device applications [9].

Recent II–VI and III–V DMS doped with magnetic ions such as Mn, Fe, Co and Ni are (CdMn)Te, (GaMn)As, (InMn)As, (GaMn)Sb, (ZnMn)O and (TiMn)O_2 [10]. The most studied DMS are (GaMn)As and (InMn)As but these are limited by Curie temperature and are unsuitable in practical spintronic devices [11]. In 2000, Dietl et al. predicted that a Curie temperature above room temperature in GaN-based DMS was possible and this has rejuvenated DMS research [12]. The successful applications of III-V nitrides in electronic and photonic devices have energized researchers to explore the potential of these materials in spintronics. The search is

still on-going, since the announcement of new DMS materials is continuously being seen in research journals and others.

Group III–V semiconducting materials, especially GaN, has attracted momentous attention because of the prediction of a T_C higher than room temperature [12] for (Ga,Mn)N doped with Mn (5 at.%). Many studies have observed ferromagnetic-like behaviour close to or higher than room temperature for (Ga,Mn)N [13, 14] and as high as 940 K by Sonoda et al. [15]. Theoretical calculations, based on local spin-density approximation, which assumed that Ga atoms were randomly substituted by magnetic atoms, have predicted diverse magnetic properties extending from spin-glass-like to ferromagnetic-like behaviour for GaN together with various concentrations of Cr, Co, Fe, Mn, Ni and V [16].

Nevertheless, GaN-based DMS with other transition metals such as Cr, Co and Ni have not been adequately investigated. Above room temperature, ferromagnetism has been observed in TiO [17] and ZnO [18] doped with cobalt ions. The implantation of various semiconductors with magnetic ions in the search for possible DMS systems has been found to be effective [19]. A few recent studies on electrical, magnetic and optical properties of cobalt ion-implanted GaN [20, 21] and ZnO [22, 23] films have been reported. However, there are not many reported experimental studies on Co^+ implanted GaN as a function of annealing temperature in the literature.

Transition metal (TM)-doped III-nitride semiconductor films are important in the emerging spintronic applications due to the observed room-temperature ferromagnetic properties [24–26]. Doping with transition metal ions also appears to be an interesting way of producing high-resistivity buffer layers in emerging III-nitride-based high electron mobility (HEMTs) transistors [27–29]. Transition metals can be introduced into group III-nitride films during growth by metal organic chemical vapour deposition (MOCVD) [30, 31]. The influence of transition metal (TM) impurities on the electrical properties of both n-GaN and p-GaN has been reported [32–34]. Hashimoto et al. [35] have grown epitaxial GaCrN films by electron-cyclotron-resonance molecular beam epitaxy (MBE). The films showed ferromagnetic behaviour with a *Tc* higher than 400 K. To the best of our knowledge, there is currently no information on the magnetization of Cr-implanted GaN, at high fluences, in the literature.

In this chapter, we present magnetic and structural properties of Co^+ and Cr^+ implanted GaN as a function of annealing temperature. Here, n-type GaN epilayers were grown on sapphire by metal organic chemical vapour deposition (MOCVD) and subsequently implanted with Co^+ and Cr^+ metal ions. The properties of Co^+ and Cr^+ implanted GaN epilayers were investigated by structural and magnetic techniques. Section 2 discusses ion implantation in semiconductors, listing some of the advantages of ion implantation compared to doping during growth; thermal annealing after ion implantation and introduces the structural and magnetic techniques used to characterize the ion implanted GaN epilayers. Section 3 briefly describes the methods and materials used and Section 4 describes, in detail, cobalt and chromium implantation in GaN epilayers.

2. Ion implantation in semiconductors

Ion implantation is a conventional doping technique for device applications. In comparison with some modern techniques for thin film growth such as MBE, the implantation process can readily be used for making selected-area contact regions for injection of spin-polarized current into device structure. The incorporation of desired atoms into semiconductor materials by ion implantation was first introduced by William Shockley. This technique was patented in U. S. in 1957 and the first commercial Ion-implanter was released on the market in the 1970s. **Figure 1** shows suitable elements in the Periodic table for implantation into semiconductors [36].

Through ion implantation, impurity ions are projected into the target material to modify its structural, optical and electronic properties. Ion implantation is a relatively simple process to introduce ions into semiconductors for doping, electrical isolation of active regions and device applications. Some of the advantages of doping by ion implantation over doping during growth are listed hereunder.

- It is a rapid means of achieving the needed fluence.
- Species of most types of ions can be introduced into essentially any host material.
- Ions can be projected to the required depth by controlling the implantation energy.

Figure 1. Periodic table elements used for ion implantation [16].

http://dx.doi.org/10.5772/68042

- A proper mask system can be used to implant ions into the desired areas of the sample.
- Desired concentrations of dopants can be implanted into the material by monitoring implantation dose which is measured by the ion current.
- Ion species can be introduced over the solid solubility limits.
- It is insensitive to the properties of the host material like sample geometry, lattice structure, lattice defects and so on.
- Doping by ion implantation is a low temperature process.

An ion implanter consists of an ion source, a mass spectrometer, high voltage accelerators, a scanning system and a target chamber. The desired implant species are usually in the form of a gas. However, vapour from a heated solid can also be used. To generate electrons, an electric potential close to 100 V is applied across the body of the chamber and the filament and the electrons emitted from the filament ionize gas atoms by impact. The exit slit is put to a potential of about –25 kV and hence positive ions are accelerated towards it. They then enter the mass spectrometer which selects ions according to their masses and charge states and allow desired ion species to pass through the exit slit of the spectrometer.

The selected ions are then accelerated by passing through the accelerating columns at high voltages. These ions pass through the pair of X and Y plates of a scanner system to produce a beam for uniform dose implantation. The scanned beam then enters the defining aperture and is projected onto the material to be implanted. Electrical contact between the target and holder allows the flow of electrons to neutralize the dopants received by the target, which are counted by the charge integrator by measuring the time averaged swept beam current according to the relation,

$$Q = \int_0^t \frac{I}{nqA}\, dt \tag{1}$$

where 'A' is the target area, 'n' is the charge state of the ion beam and 'I' is the beam current summed over the duration of implantation. A small positive potential is used to bias the target to reduce errors from secondary electrons. The energy of ions accelerated towards the target depends on the applied electrostatic potential and is known as the implantation energy. The implantation energy is normally in the range 1–2000 keV, depending on the implanter set-up. The number of ions received by the target per unit area (ions cm^{-2}) is known as dose or fluence and is measured electronically by a charge integrator.

During Coulombic interactions with target atoms, the incident ion beam loses its energy through scattering. If the complications of many-body interactions are disregarded, the supposition of binary collisions can be used as a suitable approximation. The implanted ion collides with a target atom, which in turn recoils and collides with other lattice atoms to start a collision cascade. The penetrating ion beam will encounter point defects (vacancy,

interstitial, substitutional, anti-site, etc.) in its path. The mechanisms through which an ion beam loses energy can be described in two ways, which are elastic or nuclear energy loss (Coulomb interaction) and inelastic or electronic energy loss (electron-electron energy transfer, excitation and ionization phenomenon) [1]. The total distance travelled by the incident ion normal to the target surface before coming to rest is called range. It is generally expressed by symbol R and is given by

$$R = \int_0^E \frac{dE}{NS(E)} \tag{2}$$

where N is the atomic density, dE is the ion energy loss and $S(E)$ is the stopping cross-section. The projected range is an important parameter and calculated by the penetration depth of the ions below the target surface. This is denoted by R_p and it is smaller than the actual distance R travelled by ions. The relationship between R and R_p is approximated as

$$R_p \approx \frac{R}{1+\frac{m_2}{3m_1}} \tag{3}$$

where m_1 and m_2 are the masses of incident and target atoms, respectively. Lateral range is described as the distance travelled by the ions along the normal to the incidence direction and is denoted by $R^{\perp}$, while the spread in R caused by energy loss mechanism fluctuations is known as straggling. Ions stop at different depths in the target, and hence to find the distribution around R_p standard deviation or straggling (usually denoted by ΔR_p) is used [37]. The Lindhard, Scharff and Schiott (LSS) theory [38] describes the range and distribution of implanted ions into the target. According to the LSS theory, the distribution of implanted ions follows a Gaussian function. The concentration of implanted ions at a certain depth x can be expressed as

$$N(x) = N_{max}\, e^{\frac{(x-R_p)^2}{2VR_p^2}}, \tag{4}$$

where N_{max} is the peak concentration of implanted ions and is given by

$$N_{max} = \frac{\Phi}{\sqrt{2\pi}\,V\,R_p} \approx \frac{0.4\Phi}{V\,R_p}, \tag{5}$$

where Φ is the ion dose in ion cm^{-2}, using this value of N_{max} we can find $N(x)$ as

$$N(x) = \frac{\Phi}{\sqrt{2\pi}\,V\,R_p}\, e^{\frac{(x-R_p)^2}{2VR_p^2}} \tag{6}$$

Computer simulation is an accurate and fast method of finding the range, distribution and damage caused by implanted ions into a target. Transport and range of ions in matter (TRIM) is an extensive Monte Carlo binary collision computer simulation code based on full quantum mechanical treatment of ion-atom collisions [37]. TRIM can provide ion distribution together with all kinetic occurrences associated with the ion's energy loss (target damage, sputtering, ionization and phonon production) in multi-layered complex target materials.

Although Gaussian distribution is a logical estimation for the depth profile of dopants, it applies almost entirely for amorphous targets. Semiconductor crystals are highly crystalline, therefore, incident ions, if and when implanted parallel to crystal axes, move through crystal planes without experiencing any collision and are extremely likely to channel into the substrate. Therefore, to prevent channelling effects during implantation, the target crystal is tilted 7° of the direction of incident beam.

http://dx.doi.org/10.5772/68042

2.1. Thermal annealing

The implantation of energetic ions into semiconductors produces defects, damages the lattice and creates local amorphous regions and disordered crystalline structures. Notwithstanding several benefits, ion implantation can damage the lattice, which can cause quenching of luminescence, band filling, narrowing of band gap and band tailing effects. These effects acutely alter electrical and optical properties of devices. It is therefore necessary to anneal the samples after implantation to recover the lattice and at the same time move the implanted ions to suitable locations for electrical, optical and magnetic activation of the dopants. The implanted samples can be heated through rapid thermal annealing (RTA) up to 1000°C or even higher for a number of seconds in a controllable way. RTA offers very quick heating rates (1000°C per minute) and short time processing and this is its leverage over conventional furnace annealing (which takes several minutes or hours). Moreover, RTA provides relatively high security, taking into account sample decomposition, since the sample is exposed to high temperatures for a very short duration. High temperature annealing of III-nitrides is mostly carried out in a nitrogen atmosphere to prevent loss of nitrogen from the surface of the samples. RTA has been found as an efficient method to improve crystal quality and repair implantation-induced damage in III-nitrides.

The three major components of an RTA processor are RTA chamber, a heating system and a temperature sensor. RTA was carried out in an RTP-300 rapid thermal processor with 13 tungsten halogen lamps (1250 W each) as the source of heat and ambient nitrogen gas flow. A K-type thermocouple embedded in the sample stage was used as a temperature sensor. The samples to be annealed were placed upside down on another GaN wafer placed on a 4-inch silicon wafer positioned on a sliding sample holder inside the RTA chamber. After placing the sample holder inside the chamber, the window was tightly closed using screws and then RTA programmed for the required temperature and duration. Semiconductors are usually annealed up to a temperature as high as 2/3 of the melting point of bulk material. Hence, an annealing temperature of about 1800°C would be required for GaN whose melting point is 2791°C. However, 1800°C is higher than the growth temperature of epitaxial semiconductors and this would make the material decompose and deteriorate. Therefore, annealing temperatures and time need careful optimization to balance lattice recovery and sample degradation. A number of trial runs were performed using different annealing conditions in the search for optimized values of time and temperature. Here, a maximum annealing temperature of 900°C was used for a duration of 2–5 min.

2.2. Analysis techniques

2.2.1. X-ray diffraction

XRD is a very valuable technique to analyse the structure of crystalline materials. It provides an effective means of identifying crystal structures and investigates lattice modifications in the implanted/annealed samples. The X-ray diffractometer uses X-rays produced from the material due to shell-shell transitions as probes for analysis. These rays are produced when high energy electrons bombard on a copper target and give out a monochromatic beam of Cu-K_{α} radiation. When X-rays hit a crystalline material they are diffracted by the planes of

the crystal. From Bragg's law, a diffraction peak is obtained only when the distance travelled by the rays after reflection from successive crystal planes differs by an integral multiple of wavelengths, in accordance with Bragg's equation:

$$2d \sin\theta = n\lambda \tag{7}$$

where d is inter-planer spacing, θ is the incident angle, λ is the wavelength of incident X-rays and n is the order of diffraction. The principle schematic diagram of an X-ray diffractometer is shown in **Figure 2**. A strong reflection or XRD peak is obtained by changing the angle θ so that the Bragg conditions are satisfied. Variation of angular positions with intensities of diffracted peaks produces a pattern peculiar to the material. Peak positions recorded in an XRD spectrogram are correlated with the peaks of known materials for phase analysis of the samples.

XRD analysis of the samples was performed using a Cu-K_α source of X-rays at room temperature by a Philips X'Pert data collector X-ray diffractometer. The crystallinity of the GaN samples was investigated in detail by carrying out $\omega/2\theta$ scans using double and triple axes diffraction. Moreover, peak broadening, tilt and twist characteristics were investigated by measuring FWHM from ω-scans of high resolution XRD. Powder diffraction XRD was carried out in 2θ ranges of 20–80° for phase analysis and detection of secondary phases in implanted samples.

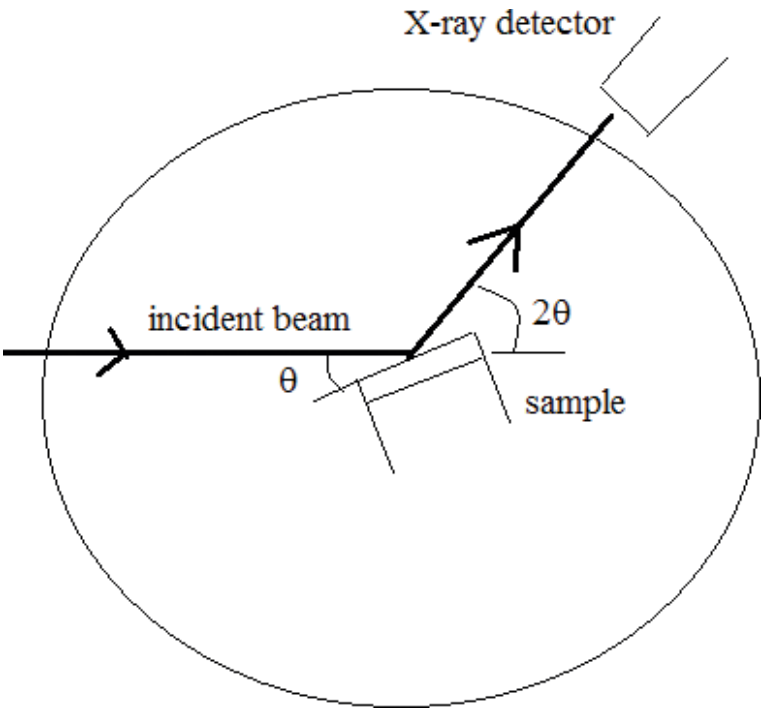

Figure 2. Principle and schematic diagram of diffractometer.

http://dx.doi.org/10.5772/68042

2.2.2. High-resolution X-ray diffraction (HR-XRD)

High resolution X-ray diffraction (HR-XRD) has long been used in the compound semiconductor industry for the characterization of epitaxial layers. The schematic diagram of HR-XRD is given in **Figure 3**.

Conventionally, HR-XRD has been employed to determine thickness and composition of epilayers, but of late the technique has progressed to enable the determination of strain and relaxation within a given layer on a multilayer structure. Typical HR-XRD symmetric reflections from a single layer on a bulk substrate are presented next.

A scan is taken by scanning sample and detector in 1:2 ratios. The substrate peak is normally the sharpest and most intense feature in the scan, also shown in **Figure 4**. The position of the Bragg peak is determined from Bragg's law. In this example, (**Figure 4**), a layer peak can be observed on the left-hand side of the substrate peak. This means that the lattice parameter of the layer is larger than that of the substrate since, from Bragg's law, it diffracts at smaller angles than the substrate. The differences in the positions of the peaks are related to the differences in lattice parameters, which can be due to composition, strain or relaxation of the layer. On both sides of the layer peak, there are interference fringes resulting from interferences of wave-fields in the layer. This information can be used for the accurate determination of the thickness of the layer.

HR-XRD measurements were performed at Beijing synchrotron radiation facility (BSRF) and Shanghai synchrotron radiation facility (SSRF). Synchrotron radiation is produced through the interaction of fast electrons with an applied magnetic field. The applied field will cause the electrons to accelerate by exerting a force on them perpendicular to their direction of motion, as shown in **Figure 5**. This will then cause the electrons to radiate electromagnetic energy

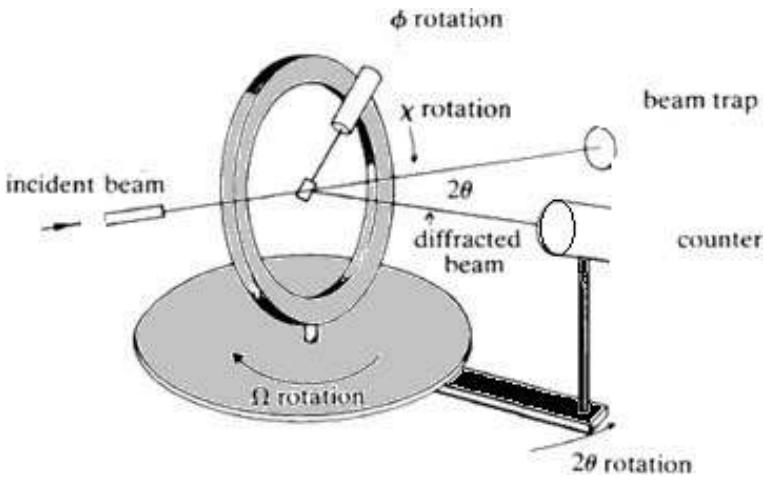

Figure 3. Principle and schematic diagram of HR-XRD.

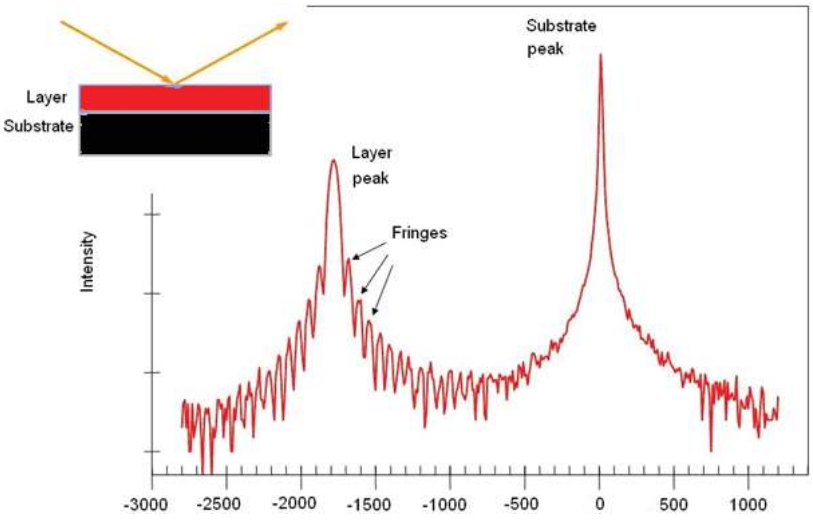

Figure 4. HR-XRD reflections from a single layer on a bulk substrate.

called magnetic bremsstrahlung or synchrotron radiation. If the energy of electrons and the magnetic field are high enough, X-rays can be produced.

2.2.3. Rutherford backscattering spectrometry (RBS)

Rutherford backscattering spectrometry (RBS) is an extensively used nuclear technique for near surface layer analysis of materials. Ions with energy in the MeV range (typically 0.5–4 MeV) bom-

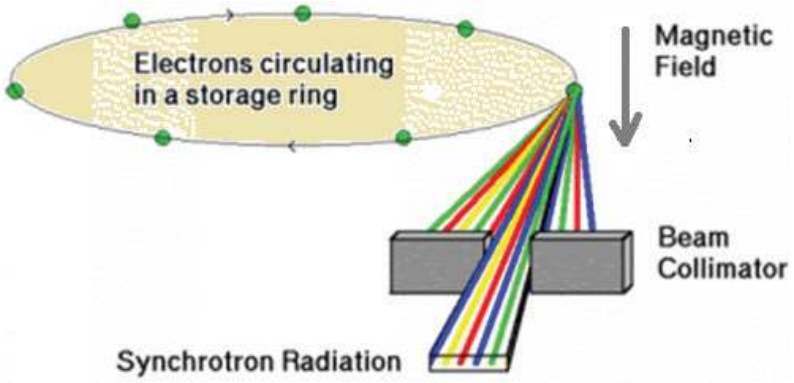

Figure 5. Principle of synchrotron radiation.

bard a target and backscatters. The energy of the backscattered ions is recorded by an energy sensitive detector, usually a solid-state detector. RBS permits the quantitative determination of material composition and a depth profile of individual elements is possible. It is quantitative without using reference samples, non-destructive and its depth resolution is good. The analysed depth is about 2 and 20 μm for He-ions and protons, respectively. The drawback of RBS is that its sensitivity for light elements is low, and this frequently requires complementing with other nuclear techniques such as nuclear reaction analysis (NRA) or elastic recoil detection analysis (ERDA).

The RBS technique is named after Sir Ernest Rutherford who, in 1911, used the backscattering of alpha particles from a gold foil to determine the fine structure of the atom, and this resulted in the discovery of the atomic nucleus. However, RBS as a materials analysis technique was first described in 1957 by Rubin et al. [39]. The book by Tesmer et al. [40] is highly recommended for further reading on modern applications of the RBS technique. RBS encompasses all forms of elastic ion scattering at incident ion energies ranging from about 500 keV to several MeV. Normally, protons, alpha particles and sometimes lithium ions are used as projectiles at backscattering angles of between 150 and 170°. There are special cases where different angles or projectiles are used. When inelastic scattering and nuclear reactions are used, the method is called nuclear reaction analysis (NRA), while detection of recoils at forward angles is called elastic recoil detection analysis (ERD or ERDA). Due to the long history of RBS, there have been many and sometimes uncontrolled growth of acronyms and a list of recommended ones can be found in Amsel [41].

2.2.3.1. Scattering geometry and kinematics

Figure 6 shows the most commonly used scattering geometries. If the incoming beam, outgoing beam and the surface normal to the sample are in the same plane, then we get the IBM geometry. And the relationship between the incident angle α, exit angle β and scattering angle θ is given by

$$\alpha + \beta + \theta = 180^{o}, \tag{8}$$

while in the Cornell configuration, the incoming beam, outgoing beam and the sample rotation axis are in the same plane, and

$$\cos(\beta) = -\cos(\alpha)\cos(\theta). \tag{9}$$

The advantage of the Cornell geometry is that it combines a large angle of scattering, which is advisable for better mass resolution, and grazing incident and exit angles, which improves depth resolution. If a projectile with incident energy E_0 and mass M_1 backscatters from a target, its energy E_1 after scattering is given in the laboratory system by

$$E_1 = K E_0, \tag{10}$$

where the kinematic factor K is given by

$$K = \frac{M_1^2}{(M_1 + M_2)^2}\left\{\cos\theta \pm \left[\left(\frac{M_2}{M_1}\right)^2 - \sin^2\theta\right]^{1/2}\right\}^2 \tag{11}$$

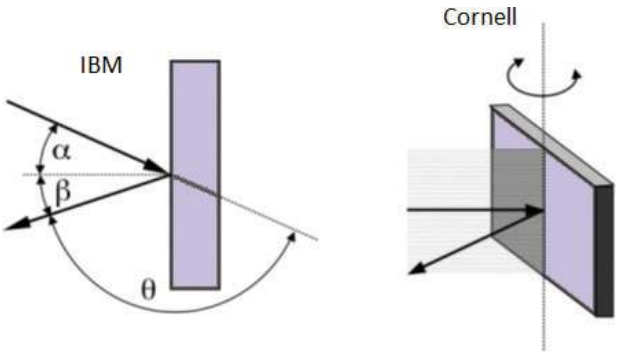

Figure 6. Left: IBM geometry; right: Cornell geometry. Incident angle α, exit angle β and scattering angle θ.

where θ is the scattering angle and M_2 is the mass of the target nucleus, initially at rest. The plus sign in above equation applies when $M_1 < M_2$. If $M_1 > M_2$ then the equation has two solutions, and the maximum possible scattering angle θ_{max} is given by

$$\theta_{max} = \arcsin\left(\frac{M_2}{M_1}\right) \tag{12}$$

Figure 7 shows the relationship between the kinematic factor and target mass for various incident ion beams.

The RBS technique uses the Rutherford scattering principle. If a high energy helium ion beam ($^4He^+$) is backscattered from a target, then the collision probability of the incident alpha particles with atoms of the target is determined by the Rutherford cross-section. If there is elastic

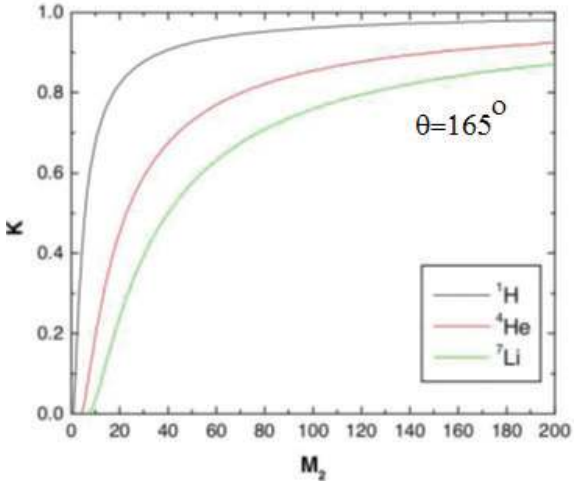

Figure 7. Kinematic factor K at a scattering angle $\theta = 165°$ as a function of target mass $M2$.

http://dx.doi.org/10.5772/68042

collision between incident alpha particles and target atoms then the energy ratio of the particles pre- and post-collision is equal to the ratio of the masses of both particles. Information on the atoms from which the alpha particles have been backscattered can be inferred from the energy of the backscattered alpha particles. According to the single scattering theory, an alpha particle faces only one large angle scattering before reaching the detector. The principle and schematic diagram of the RBS technique is shown in **Figure 8**. This approximation helps to convert the energy scale into the depth scale of the sample within the energy resolution of the detector. The lower the energy of the backscattered alpha particles, the deeper the detected atoms.

In this study, an alpha beam of energy 2 MeV with a diameter of 1 mm was used. The samples were mounted on a two axis goniometer, which can align the sample with the incident beam at any angle required. There are two silicon detectors in the target chamber. One detector is used to measure particles backscattered at angles near the incident beam and the second detector is for particles backscattered at glancing angles to the sample surface. The second detector, set at 165° relative to incident beam direction and 80 mm away from the sample, has a resolution of 18 keV and an aperture diameter of 5 mm. The RBS data was analysed using RUMP simulation.

2.2.4. AGM and SQUID

To manipulate magnetic materials, it is very important to know their magnetic moments and this can be measured with the alternating gradient magnetometer (AGM). Although AGM is extremely sensitive, it cannot measure single magnetic markers directly. Alternatively, the average magnetic moment for a single bead is calculated from measurements of several millions of markers. Additionally, the number of measured magnetic markers cannot be counted exactly, but only estimated by the given dilution. The magnetic moment at a small outer field (~100 Oe), not the moment for saturated magnetic beads, is interesting for bond-force measurements. Apart from that only the mean magnetic moment of the beads should be known, more problems were found during measurements. Although the beads are superparamagnetic, some of them show remanent magnetization. This could be due to clustering of the beads, not fully oxidized magnetite (Fe_3O_4) particles inside the beads or a few very big beads. In order to prevent clustering, the magnetic markers are pipette spotted onto a heated Si-wafer (~100). Clustering could not have been the sole reason for ferromagnetic behaviour since the effect remained. Furthermore, the magnetic moment

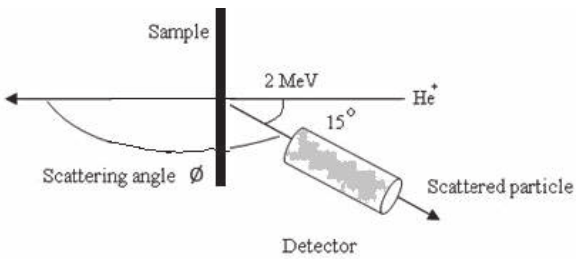

Figure 8. Principle and schematic diagram of RBS.

shows dependency on bead concentrations, which cannot be neglected (six different concentrations were tested for every bead type). All of this has to be considered when calculating the magnetic moment at a small outer magnetic field.

SQUID magnetometry is a very sensitive technique for magnetic characterization of materials. A SQUID can detect magnetic ordering by tracking temperature dependency on magnetization (MT), field-dependent magnetization (MH) and very weak magnetic moments. A SQUID works on the principle of electron-pair wave coherence and Josephson effect, which can be defined as the flow of current (called Josephson's current) across two superconductors separated by an insulated layer. A Josephson's junction comprises two superconducting coils separated by a very thin insulating barrier to enable electrons to pass through it. A SQUID magnetometer is made of a superconducting ring into which two Josephson's junctions are placed in parallel in a magnetic field. A current flows through the superconducting loop if a magnetic field is applied. The magnetic flux of a ferromagnetic sample placed between the superconductors in the presence of an applied field will change accordingly. This magnetic flux change will induce a current which changes the initial current circulating through the coil. The variation in the current helps to detect the magnetic moment of the material.

Figure 9 shows the principle of SQUID magnetometry. A SQUID magnetometer was used to investigate MT and MH characteristics of metal ion-implanted GaN samples. During MH analysis, the hysteresis loops of ion-implanted and unimplanted samples were recorded at

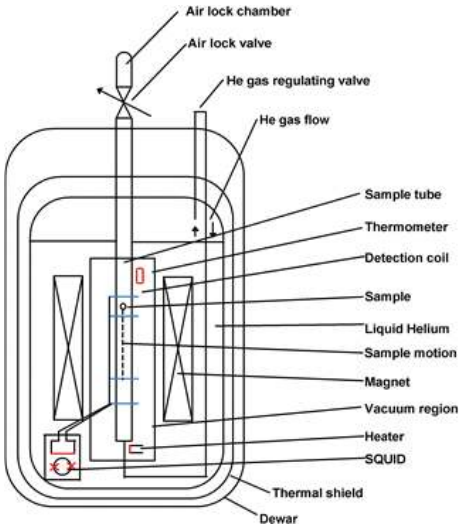

Figure 9. Schematic diagram of a typical SQUID magnetometer [42].

http://dx.doi.org/10.5772/68042

100 and 300 K, respectively. For MT measurements, the sample was first cooled down to 5 K with no applied magnetic field. A 500 Oe magnetic field was then applied and a scan collected up to 350 K to obtain a zero field cooled (ZFC) trace. Secondly, the sample was cooled down to 5 K in the 500 Oe field and magnetization measured to get the field cooled (FC) trace. The surface of the sample was kept parallel to the applied magnetic field during magnetization measurements.

3. Methodology and materials

Epitaxial layers of GaN (n-type) about 2 μm thick were grown on sapphire (Al_2O_3) by metal organic chemical vapour deposition (MOCVD). The structure and crystal quality of the GaN epilayers were analysed by Rutherford backscattering and channelling spectrometry (RBS/C) prior to ion implantation. A He^+ ion beam, with energy 2.0 MeV, was used for RBS/C analysis. Sample mounting and detector specifications and configurations have already been explained in Section 2.2. The <0001> normal axis was chosen to investigate the quality of GaN. The channelling minimum yield was found to be around 1.3%, indicating that the quality of the epitaxial GaN material was high. Co^+ ions of energy 150 keV were implanted into the GaN epilayers at room temperatures at doses of 3×10^{16} and 5×10^{16} ions cm^{-2}, making the wafer to self-heat at such high doses. This is advantageous since it causes 'dynamic annealing', that is, annealing during implantation. The concentration of cobalt was calculated to be around 3–5% from SRIM 2008 [37]. The estimated range of Co^+ ions in the sample was approximately 150 nm. The implanted samples were annealed at 700, 800 and 900°C for 5 min using rapid thermal annealing (RTA) in an ambient N_2 atmosphere to remove implantation damage and recrystallize them. Similarly, Cr^+ ions of energy 150 keV were implanted into the GaN epilayer at room temperature to a dose of 3×10^{16} ions cm^{-2} at a tilted angle of 7^o of the direction of incident beam to avoid implantation channelling effects. The chromium concentration was estimated to be about 3% as calculated from SRIM 2008 and also confirmed by simulation of random spectra using RUMP. The projected range of the Cr^+ ions in the samples was about 150 nm. The implanted samples were annealed at 800 and 900°C for 2 min using rapid thermal annealing (RTA) in ambient N_2 to re-crystallize the samples and to remove implantation damage.

X-ray diffraction (XRD, Philips X'Pert Data Collector) was used for structural analysis of ion-implanted samples, using Cu K_α radiations. High resolution X-ray diffraction (HR-XRD, BEPCII-2.5 GeV) was performed at Beijing synchrotron radiation facility (BSRF) and at Shanghai synchrotron radiation facility (SSRF). Alternating gradient magnetometry (AGM, PMC 2900-04C) was used for measuring magnetization at room temperature and a superconducting quantum interference device magnetometer (MPMS-XL Quantum Design) was used to investigate magnetic properties at 5 K. A magnetic field was applied parallel to the sample surface during magnetization measurements.

4. Metal ion implantation into GaN

Cobalt ions were implanted into GaN at doses of 3×10^{16} and 5×10^{16} ions cm^{-2} and chromium ions were implanted at a dose of 3×10^{16} ions cm^{-2}.

4.1. Cobalt implantation into GaN

4.1.1. X-ray diffraction (XRD)

Typical XRD spectra of GaN for as-grown and all the implanted samples annealed at 700, 800 and 900°C are given in **Figures 10** and **11**. **Figures 10** and **11** show typical XRD profiles of Co^+ implanted GaN at 3×10^{16} and 5×10^{16} ions cm^{-2} and subsequently annealed at 700, 800 and 900°C. In the as-grown sample, three main peaks appeared corresponding to the expected diffraction from the GaN epilayer and sapphire substrate structure.

Comparison of the XRD patterns of the as-grown with the implanted samples at different doses, it can be observed that no secondary phases or metal-related peaks were detected in the as-implanted samples and annealed samples. The diffraction patterns show peaks corresponding to the GaN layer and the substrate structure only. However, the presence of sufficiently small cobalt nanoscale precipitates, which cannot be detected by XRD due to its insensitivity on the nanoscale [43, 44], is possible.

HR-XRD ($\theta - 2\theta$) spectra showing the (0002) peak of GaN for the as-grown and selected implanted samples at doses 3×10^{16} and 5×10^{16} ions cm^{-2} and annealed at 900°C are given in **Figures 12** and **13**. In **Figure 12**, the diffraction pattern of the implanted sample, a typical satellite peak appears at lower side of the main GaN (0002) reflection. Ion implantation into crystalline GaN introduces lattice disorder which is a side effect of implantation [4]. As a result, in addition to GaN peak, new peak/peaks, representing the damaged part of lattice, appear on the low angle side of the main GaN peak in the XRD spectra of implanted GaN as reported by many researchers [45–49].

The shape, position and number of such new peaks were found to differ for different ions implanted into GaN. Most of the authors attributed such new XRD peaks to the implantation induced strain and the expansion of GaN lattice in the implanted portion of the material [45–48]. Another group of researchers suggested that these peaks were related to the formation of new phases [49]. Liu et al. presented a comparative XRD study of Ca- and Ar-implanted GaN and observed larger lattice expansion for Ar implantation. They assigned the observed phenomenon to the inability of inert gas ions to occupy substitutional sites in the lattce [45]. Inert gases, due to their very low solubility in solids, are reported to produce small gas-vacancy clusters that lead to the formation of gas-filled cavities called bubbles [50]. The formation of such inert gas cavities was also observed in several other materials such as Si [51], GaAs [52], SiC [53] and InP [54]. These empty cavities, due to their negative curvatures, contain high density of dangling bonds that exhibit high affinity for metallic contaminants and can act as impurity gettering sites [55]. Gettering of oxygen impurity atoms and structural defects in GaN by helium implantation has been reported [55–57].

http://dx.doi.org/10.5772/68042

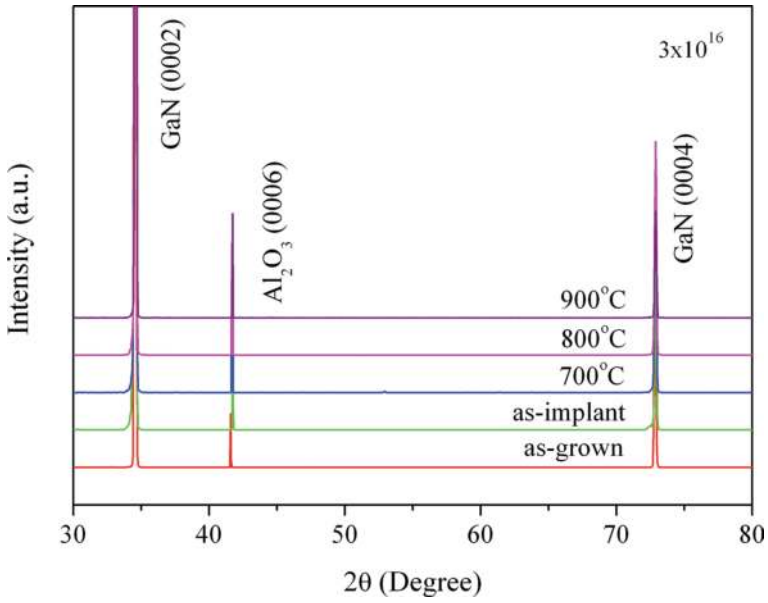

Figure 10. Typical XRD pattern of Co+ implanted at dose 3×10^{16} cm^{-2} [66].

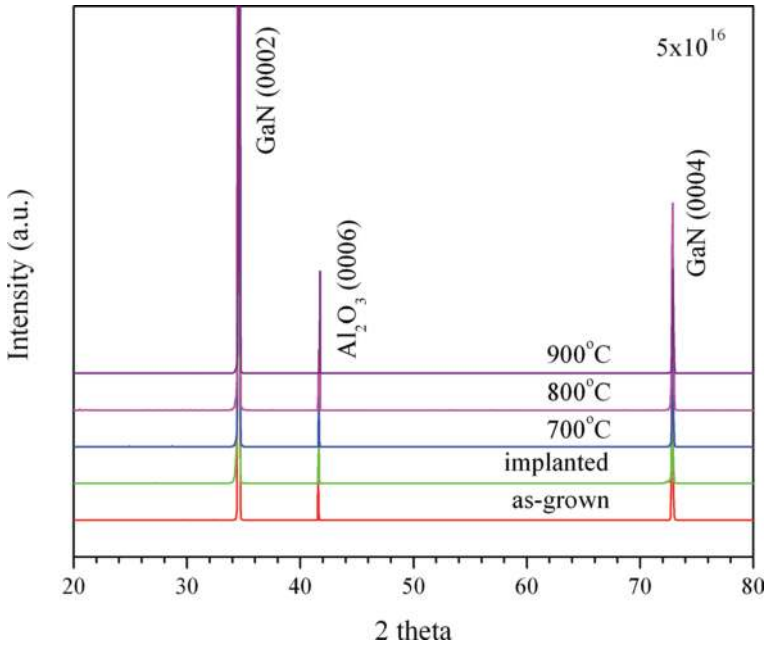

Figure 11. Typical XRD pattern of Co+ implanted at dose 5×10^{16} cm^{-2} [67].

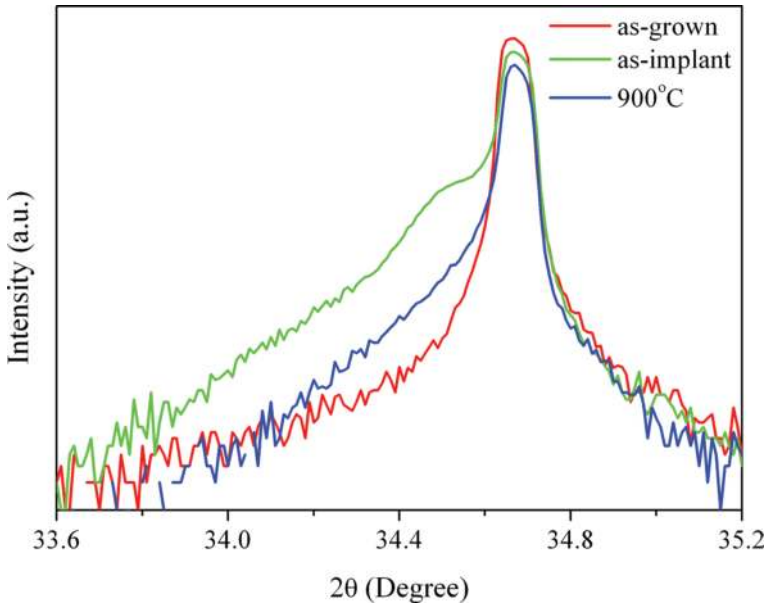

Figure 12. HR-XRD pattern of Co+ implanted at 3×10^{16} ions cm^{-2} [66].

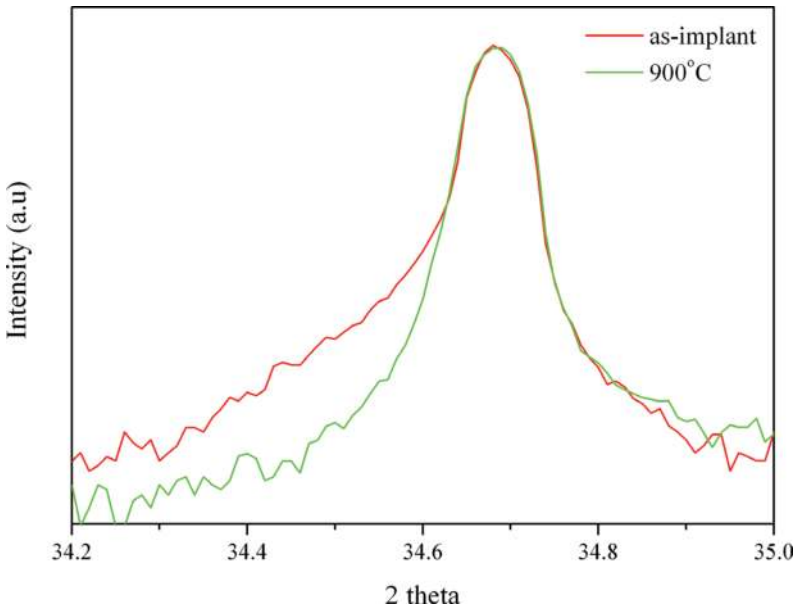

Figure 13. HR-XRD pattern of Co+ implanted at 5×10^{16} ions cm^{-2} [67].

http://dx.doi.org/10.5772/68042

The presence of similar peaks has previously been observed in the XRD spectra of GaN implanted with different ions and is thought to be due to lattice expansion along the *c*-axis of GaN [45, 46]. The new peak from HR-XRD measurements is attributed to implantation-induced damage and also to the formation of $Ga_{1-x}Co_xN$ on the part of the sample which was implanted. A shoulder peak observed on the left side of the GaN peak on XRD scans of MBE grown samples has been attributed to the GaMnN phase by Cui and Li [58]. The lattice constant of (Ga,Co)N varies with cobalt incorporation, implying that the position of the new peak is related to the amount of cobalt in the material. Hence, the introduction of cobalt at interstitial and substitutional sites in GaN is expected to cause lattice expansion to produce a new XRD peak on the left side of the GaN peak [59]. The shifting of additional peaks to the right with annealing, presented in both **Figures 12** and **13**, points to lattice recovery and improvement in the uniformity of GaCoN which may be due to increase in the substitution probability of cobalt atoms.

4.1.2. RBS channelling

The RBS channelling spectrum of the as-grown GaN/sapphire (0001) together with the corresponding minimum channelling yield χ_{min} = 1.3%, indicating high crystalline quality [60, 61], is shown in **Figure 14**.

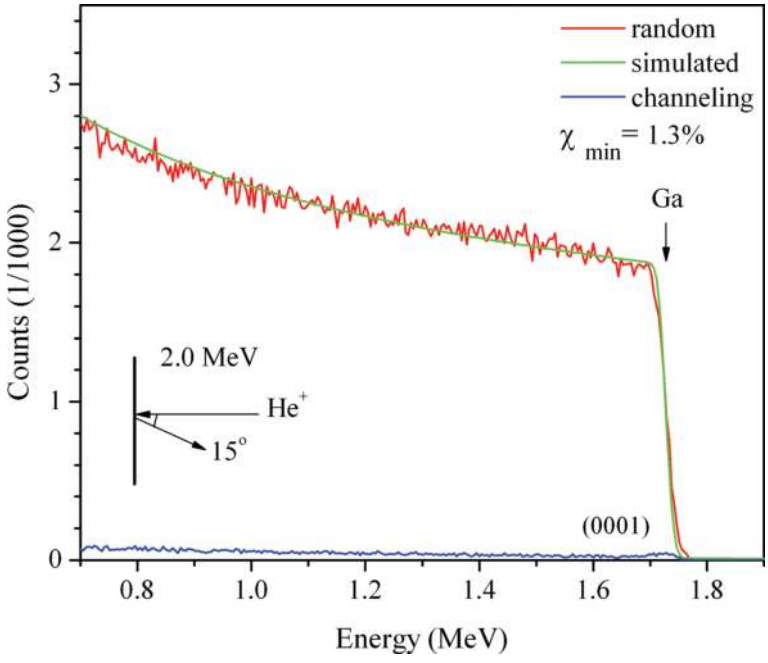

Figure 14. RBS/C of as-grown sample along with the backscattering geometry [66].

A random spectrum simulation was carried out using the RUMP program [62]. Channelling spectra are presented in **Figures 15** and **16** for Co^+ implanted GaN sample at doses of 3×10^{16} and 5×10^{16} ions cm^{-2} and subsequently annealed samples at 700, 800 and 900°C along with the corresponding minimum channelling yields χ_{min}. **Figures 15** and **16** present minimum channelling yields χ_{min} calculated for the maximum at around 1.64 MeV and is related to the random spectrum of virgin (upper spectrum) GaN.

The random spectrum of the as-implanted GaN is not shown here due to minor differences with the random spectrum of as-grown GaN. Co^+ implanted GaN sample at doses 3×10^{16} and 5×10^{16} ions cm^{-2} and subsequently annealed at 900°C showed better recovery of implantation damage. From our measurements, annealing at 900°C is the most suitable annealing temperature to re-crystallize the samples.

4.1.3. AGM and SQUID

Magnetization against magnetic field (M-H) curves from AGM measurements at room temperature for the samples implanted at doses of 3×10^{16} and 5×10^{16} ions cm^{-2} and subsequently annealed at 700, 800 and 900°C are shown in **Figures 17** and **18**, where the signal from the sapphire substrate (diamagnetic) was extracted. The magnetic field was applied parallel to the sample plane. Well-defined hysteresis loops were observed even at 300 K. The saturation field was about 4000 Oe and the coercivity H_c was about 100 Oe for the implanted and annealed samples. These results confirm that the samples were ferromagnetic even at room temperature.

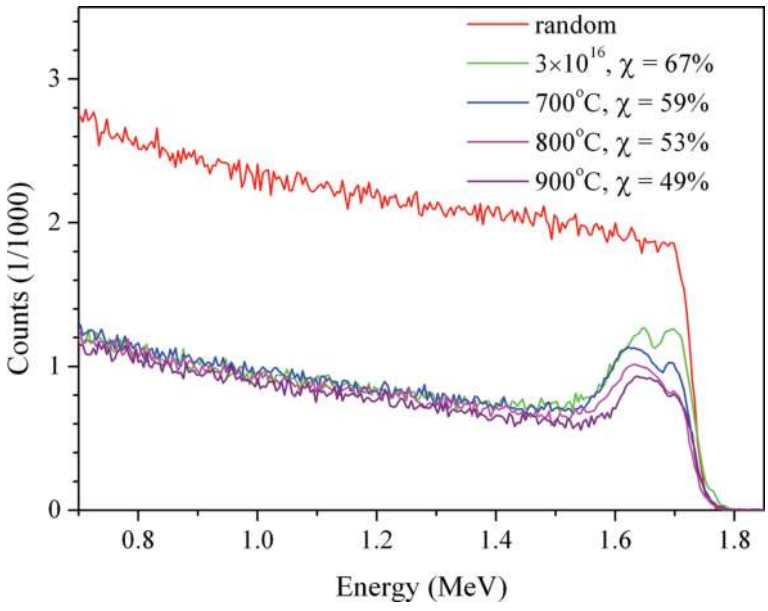

Figure 15. RBS/C of Co+ implanted GaN at 3×10^{16} ions cm^{-2} and annealed samples at different temperatures [66].

http://dx.doi.org/10.5772/68042

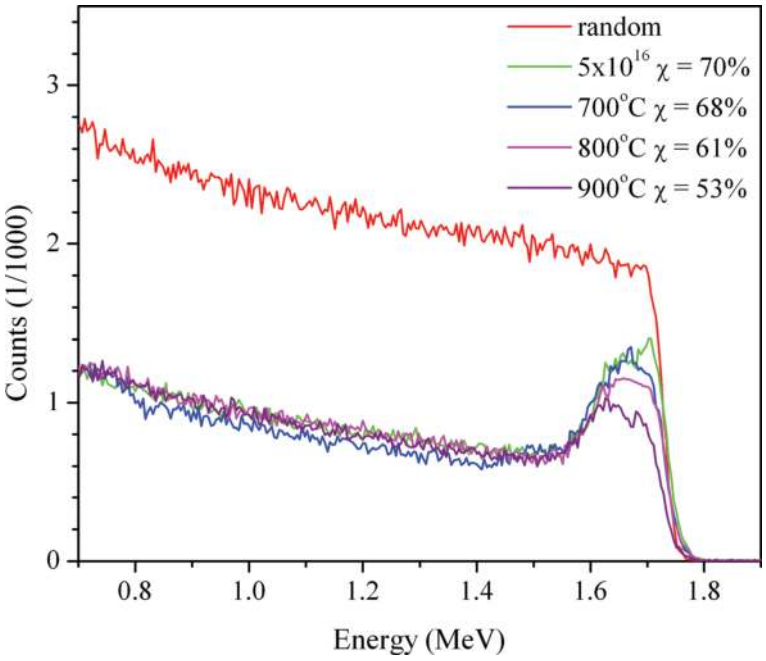

Figure 16. RBS/C of Co+ implanted GaN at 5×10^{16} ions cm^{-2} and annealed samples at different temperatures [67].

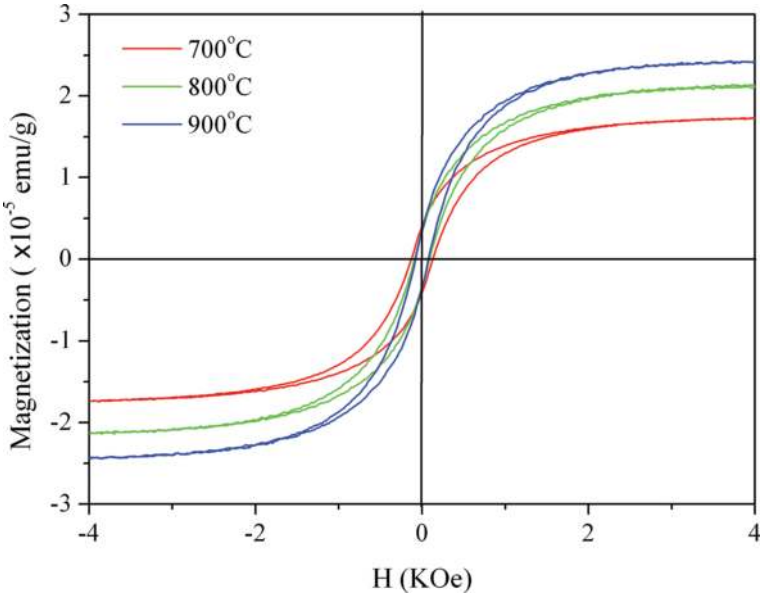

Figure 17. M-H loops at 300 K of sample implanted at dose 3×10^{16} ions cm^{-2} and annealed [66].

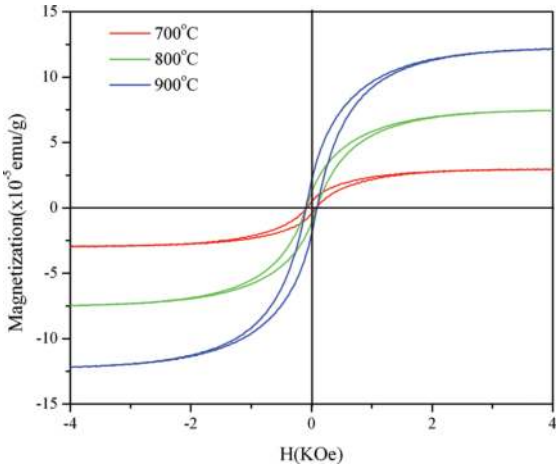

Figure 18. M-H loops at 300 K of sample implanted at dose 5 × 10^{16} ions cm^{-2} and annealed [67].

Similarly, a well-defined hysteresis loop, measured using a SQUID magnetometer, at 5 K was also observed from samples implanted at a dose of 3 × 10^{16} ions cm^{-2} and subsequently annealed at 700, 800 and 900°C as shown in **Figure 19**. The saturation field was about 4000 Oe and the coercivity H_c was about 180 Oe for implanted and annealed samples at 700 and 800°C and the coercivity was observed around 270 Oe for the sample annealed at 900°C. Also, a well-defined hysteresis loop at 5 K from SQUID was also observed for the samples implanted at a dose of 5 ×10^{16} ions cm^{-2} and subsequently annealed at 700, 800 and 900°C as shown in **Figure 20**. The saturation field was about 4000 Oe and the coercivity *Hc* was about 270 Oe for implanted and annealed samples at 700 and 800°C and the coercivity was observed around 600 Oe for the sample annealed at 900°C.

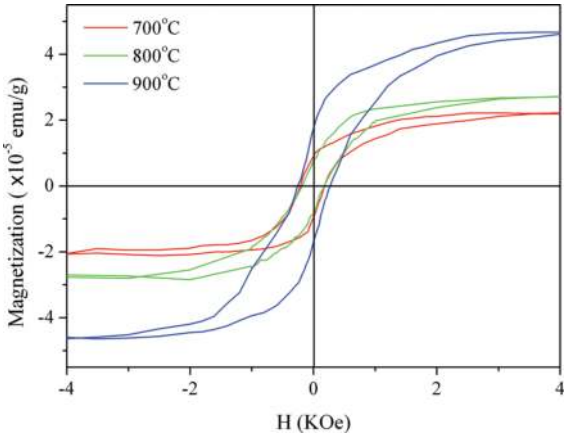

Figure 19. M-H loops at 5 K of sample implanted at dose 3 × 10^{16} ions cm^{-2} and annealed [66].

http://dx.doi.org/10.5772/68042

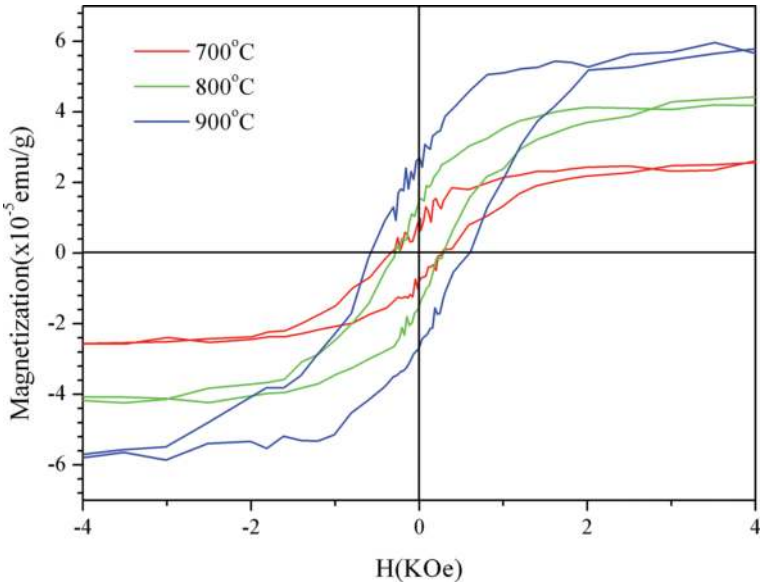

Figure 20. M-H loops at 5 K of sample implanted at dose 5 × 10^{16} ions cm^{-2} and annealed [67].

Magnetization as a function of temperature for selected samples is plotted in **Figures 21** and **22**. The variation of magnetization with temperature indicates multiple exchange interactions,

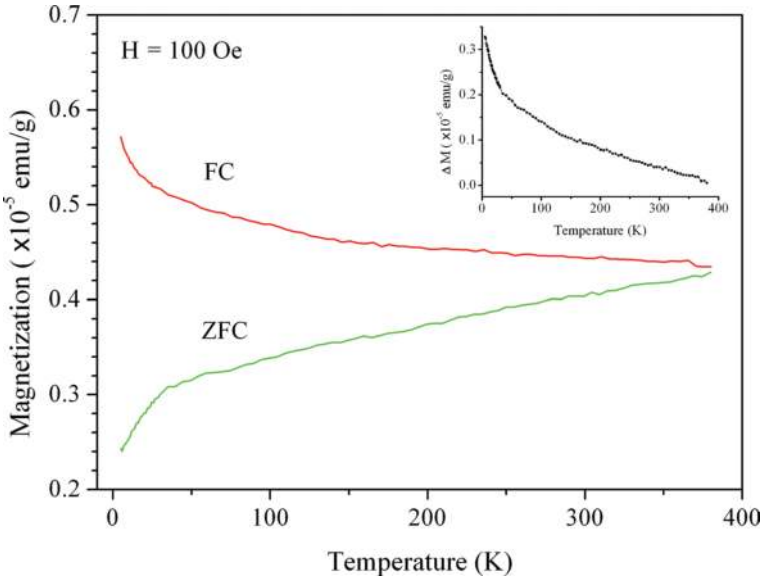

Figure 21. FC/ZFC measurements of sample implanted at a dose of 3 × 10^{16} ions cm^{-2} and annealed at 900°C [66].

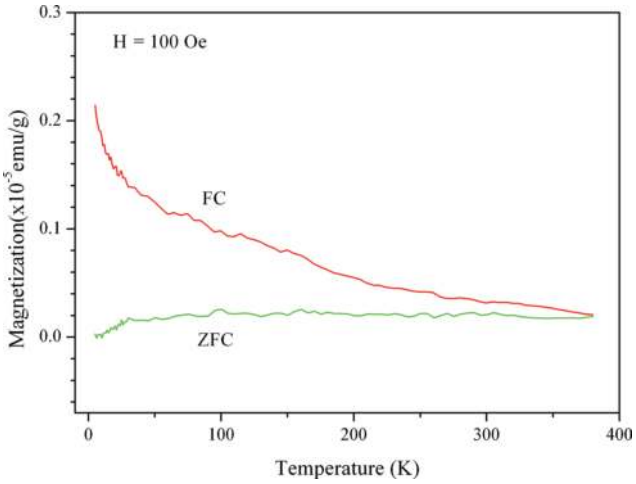

Figure 22. FC/ZFC measurements of sample implanted at a dose of 5 × 10^{16} ions cm^{-2} and annealed at 900°C [67].

indicating that its decay cannot be easily fit to classical description of ferromagnetism, again in agreement with current theories concerning DMS systems with low carrier concentrations. Co^{+} implanted GaN at doses of 3 × 10^{16} and 5 × 10^{16} ions cm^{-2} and annealed at 900°C showed magnetic moment at lower temperatures and retained magnetization up to 370 K. There were indications of the possible presence of multiple complex exchange interactions for Co^{+} implanted GaN. The same phenomenon has been observed on Cr^{+} implanted GaN.

All samples exhibited well-saturated MH loops (**Figures 17–20**) with finite coercivity, eliminating the likelihood of both paramagnetism and superparamagnetism [63]. Analysing hysteresis loops of the implanted samples assists in the investigation of the magnetic properties of the material. Lateral shifting of hysteresis loop was not observed, and this eliminates spin glass behaviour [64]. These observations imply that there was ferromagnetic ordering in implanted samples at room temperature. No extra peaks were observed on the XRD spectra of the implanted samples (**Figures 10** and **11**), reducing the contributions of secondary phases (Co_xN_y, CoGa, etc.) to the observed ferromagnetism. FC and ZFC measurements were performed on a representative sample, together with magnetization as a function of temperature, and the data did not show any blocking temperature that can be related to superparamagnetic behaviour arising from undetected magnetic secondary phase clusters.

4.2. Chromium implantation into GaN

4.2.1. X-ray diffraction (XRD)

Typical XRD spectra of GaN for the as-grown and Cr^{+} implanted at a dose of 3 ×10^{16} ions cm^{-2} and subsequently annealed at 800 and 900°C are given in **Figure 23**. In the as-grown sample, the three main peaks correspond to the expected diffraction from the GaN epilayer and sapphire substrate structure.

http://dx.doi.org/10.5772/68042

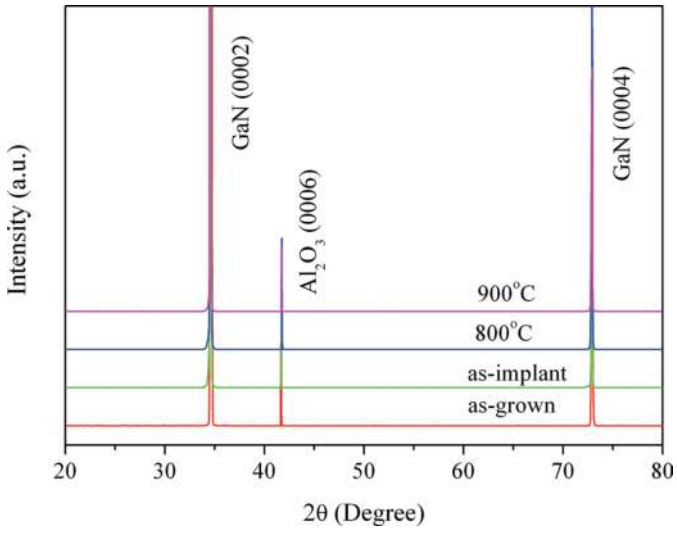

Figure 23. Typical XRD pattern for the as-grown, implanted and annealed samples at different temperatures.

XRD did not show any secondary phases or metal-related peaks on the as-implanted samples and annealed samples, when compared with the as-grown sample. Only peaks corresponding to the GaN layer and the substrate structure could be observed on the diffraction pattern. However, the presence of sufficiently small chromium nanoscale precipitates, which cannot be measured by typical XRD due to its insensitivity on the nanoscale [43, 44], is not excluded. HR-XRD spectra of GaN for implanted samples at a dose of 3×10^{16} ions cm^{-2} and annealed at 900°C are given in **Figure 24**. In the diffraction pattern of the implanted sample, a typical satellite peak appears at the lower side of the main GaN (0002) reflection.

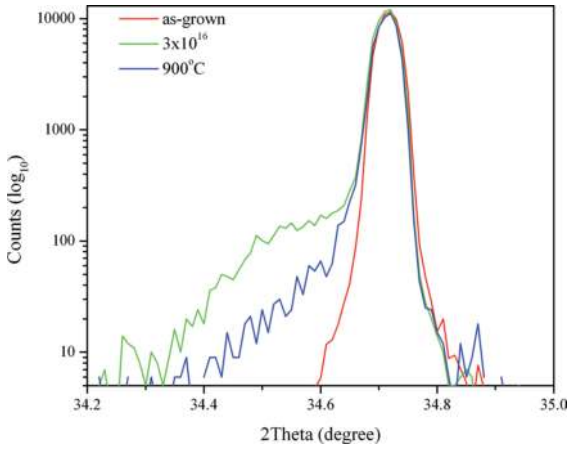

Figure 24. 2 HR-XRD spectra for Cr+ implanted GaN and subsequently annealed at 900°C [68].

The shape, position and number of such new peaks were found different as observed in Co^+ implanted GaN epilayers. The new peak in the XRD scans is assigned to implantation-induced damage as well as the formation of $Ga_{1-x}Cr_xN$ in the implanted part of the sample. The lattice constant of (Ga,Cr)N changes due the presence of chromium, implying that the position of the new peak is related to the concentration of chromium in the material. Hence, the introduction of chromium at interstitial and substitutional sites in GaN is expected to cause lattice expansion to produce a new XRD peak on the left side of the GaN peak [59]. The shifting of additional peaks to the right with annealing, presented in **Figure 24**, points to lattice recovery and improvement in the uniformity of GaCrN which may be due to increase in the substitution probability of chromium atoms.

4.2.2. RBS channelling

Channelling spectra are presented in **Figure 25** for Cr^+ implanted GaN sample at dose 3×10^{16} ions cm^{-2} and subsequently annealed at 800 and 900°C along with the corresponding minimum channelling yield χ_{min}. A minimum channelling yield χ_{min} was calculated for the maximum at around 1.65 MeV and is related to the random spectrum of the as-implanted sample (upper spectrum). Cr^+ implanted GaN sample at dose 3×10^{16} ions cm^{-2} and annealed at 800 and 900°C showed the recovery of implantation damage. If we compare these results with Co^+ implanted samples at same dose, we observe that there is less recovery of implantation damage by annealing using RTA for Cr^+ implanted samples. This may have been due to shorter annealing time (2 min).

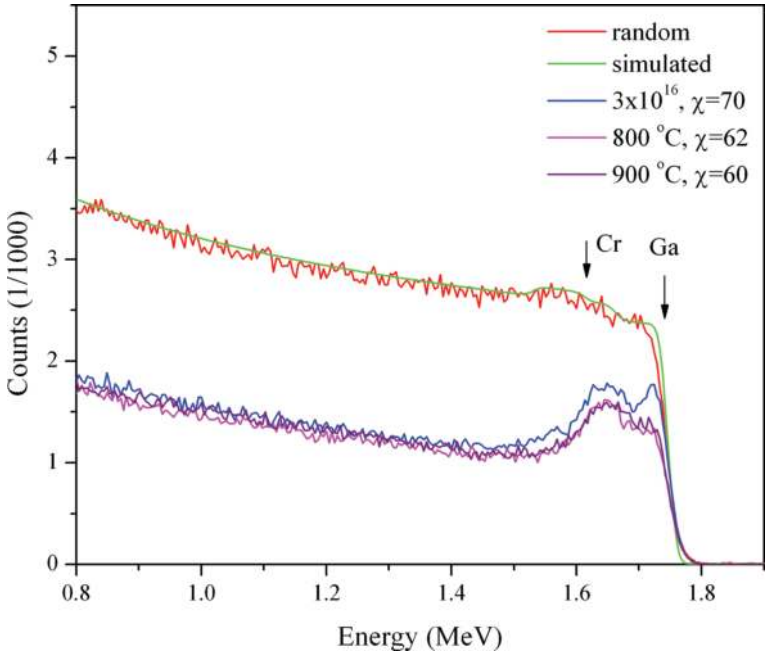

Figure 25. RBS/C of as-implanted sample at 3×10^{16} ions cm^{-2} and annealed at 800 and 900°C [68].

http://dx.doi.org/10.5772/68042

4.2.3. AGM and SQUID

Magnetization versus magnetic field (M-H) curves from AGM measurements at room temperature for the sample implanted to a dose of 3 ×10^{16} ions cm^{-2} and annealed at 800 and 900°C are shown in **Figure 26**, where the signal from the sapphire substrate (diamagnetic) was extracted. The magnetic field was applied parallel to the sample plane. At 300 K, a well-defined hysteresis loop was observed, which provides evidence for the presence of ferromagnetic interactions at room temperature. The saturation field was about 4000 Oe and the coercivity H_c was about 100 Oe for the implanted and subsequently annealed samples. These results confirm that the samples were ferromagnetic even at room temperature. Comparison with same dose for Co^+ implanted samples shows that the saturation magnetization *Ms* values are almost the same in all samples.

Similarly, a well-defined hysteresis loop at 5 K from SQUID was also observed for the implanted and subsequently annealed samples at 800 and 900°C, as shown in **Figure 27**. The saturation field is about 4000 Oe and the coercivity H_c is about 175 Oe for implanted and annealed samples. If we compare the results at 5 K with the same dose of Co^+ implanted samples we find that the saturation magnetization *Ms* values are almost similar for the sample annealed at 800°C. But the *Ms* value for Cr^+ implanted sample annealed at 900°C is 10.7 (×10^{-5} $emug^{-1}$) while for the Co^+ implanted it is about 4.5 (×10^{-5} $emug^{-1}$). A higher value of *Ms* for Cr^+ implanted GaN epilayer annealed at 900°C suggests that samples implanted with Cr^+ ions may perform better for dilute magnetic semiconductors (DMSs) compared to Co^+ implanted. Also higher values of *Ms* for implanted samples may suggest that 900°C is a suitable annealing temperature for the activation of dopants.

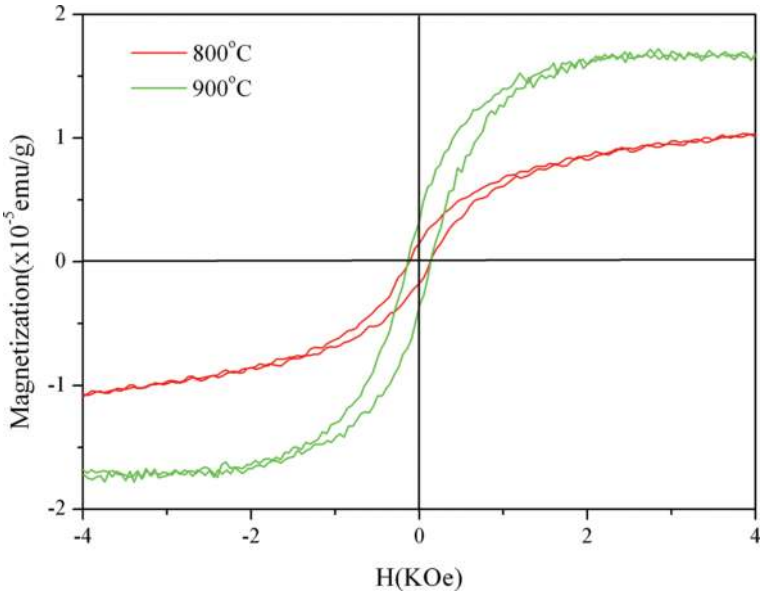

Figure 26. M-H loops at 300 K of sample implanted at dose 3 × 10^{16} ions cm^{-2} and annealed [68].

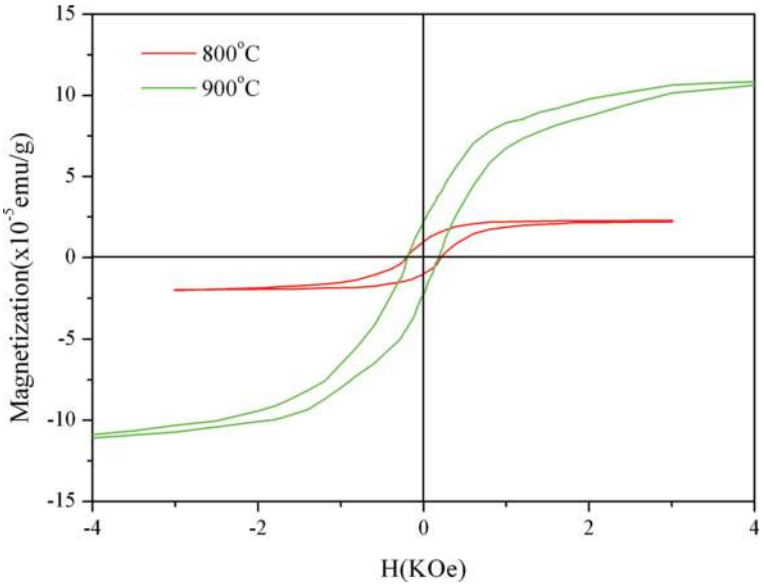

Figure 27. M-H loops at 5K of sample implanted at dose 3 × 10^{16} ions cm^{-2} and annealed [68].

Figure 28 shows magnetization as a function of temperature for Cr^{+} implanted GaN at 3 ×10^{16} ions cm^{-2}, with multiple exchange interactions indicating that its decay cannot be easily fit to classical description of ferromagnetism, again in agreement with current theories concerning DMS systems with low carrier concentrations. The Cr^{+} implanted GaN at 3 ×10^{16} ions cm^{-2} and annealed at 900°C showed magnetic moment at lower temperatures, retaining magnetization above the measured temperature of 380 K. This observation is consistent with the epitaxial prepared (Ga,Cr)N magnetic properties observed by Hashimoto et al. who have reported T_C higher than 400 K [35]. The value of *Ms* was higher for the sample annealed at 900°C compared to the sample annealed at 800°C. This increase is assumed to be due to the increase in Cr concentration on Ga sites. These observations suggest that annealing at 900°C is suitable for proper activation of Cr in GaN, which is also supported by the observations reported by Hwang et al. [65].

Well-saturated MH loops were observed in all samples (**Figures 26** and **27**) with finite coercivity, eliminating the likelihood of both paramagnetism and superparamagnetism [63]. Analysing hysteresis loops of the implanted samples assists in the investigation of the magnetic properties of the material. Lateral shifting of hysteresis loop was not observed, and this eliminates spin glass behaviour [64]. These observations imply that there was ferromagnetic ordering in implanted samples at room temperature. No extra peaks were observed on the XRD spectra of the implanted samples (**Figures 23**), reducing the contributions of secondary phases (Cr_xN_y, CrGa, etc.) to the observed ferromagnetism. Along with magnetization as a function of temperature measurements, FC and ZFC measurements were made on a representative sample and the data did not indicate any blocking temperature that

http://dx.doi.org/10.5772/68042

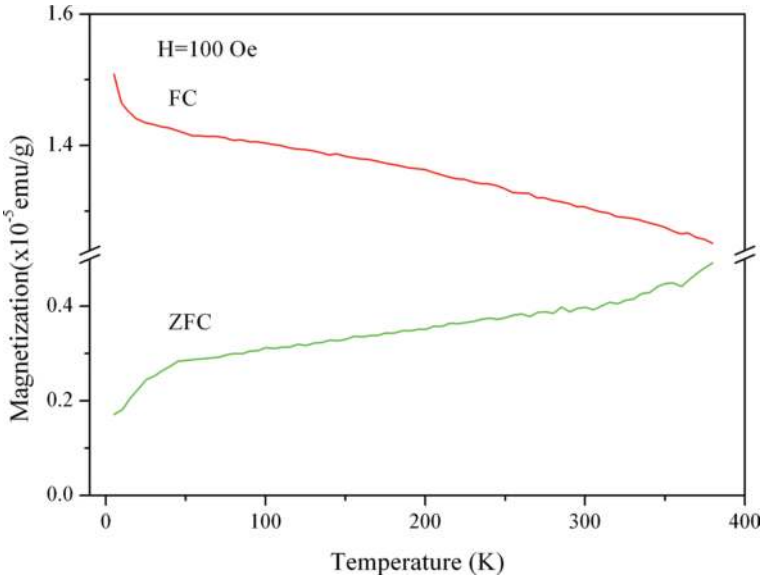

Figure 28. FC/ZFC measurements of the sample implanted at 3 × 10^{16} ions cm^{-2} and annealed at 900°C [68].

can be associated with superparamagnetic behaviour arising from undetected magnetic secondary phase clusters. **Figure 29** presents FC-ZFC measurements for Co^{+} and Cr^{+} ions implanted with the same dose and annealed at 900°C, which also suggests that Cr^{+} ions are much suitable for the fabrication of dilute magnetic semiconductors (DMS).

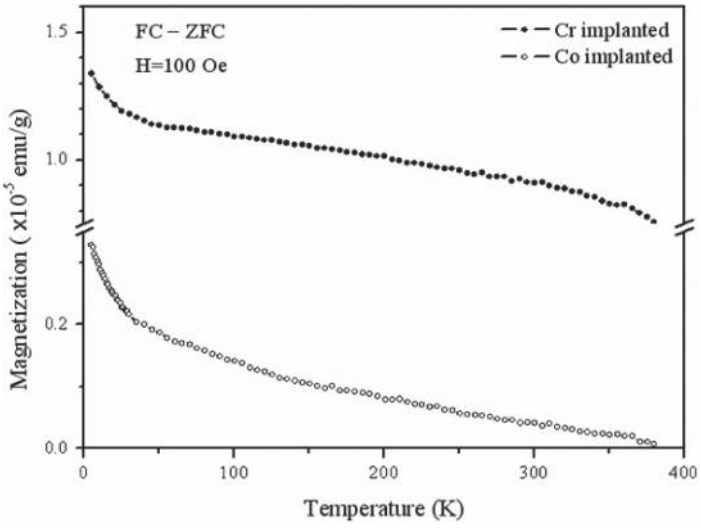

Figure 29. FC-ZFC of Co+ and Cr+ implanted samples at 3 × 10^{16} ions cm^{-2} and annealed at 900°C.

5. Conclusion

1. RBS/C measurements on the as-grown GaN samples showed good crystalline quality (χ_{min} = 1.3%) and ion-implanted samples showed recovery of lattice damage after annealing by RTA at different temperatures.

2. Typical XRD profiles were taken for Co^+ implanted GaN at doses 3 ×10^{16} and 5 ×10^{16} ions cm^{-2} and subsequently annealed at 700, 800 and 900°C and for Cr^+ implanted GaN at a dose of 3 × 10^{16} ions cm^{-2} and subsequently annealed at 800 and 900°C. In the as-grown samples, three main peaks appeared, corresponding to the expected diffraction from the GaN epilayer and sapphire substrate structure. Comparison of as-grown with the implanted samples at different doses showed that no secondary phase or metal-related peaks were detected in the as-implanted samples and annealed samples from typical XRD spectra. The diffraction patterns only showed the presence of peaks corresponding to the GaN layer and the substrate structure.

3. On diffraction patterns from HR-XRD scans of implanted samples, typical satellite peaks appear at lower side of the main GaN (0002) reflection. The new peaks on the HR-XRD scans are assigned to implantation-induced damage as well as the formation of $Ga_{1-x}Co_xN$ or $Ga_{1-x}Cr_xN$ in the implanted part of the samples. The lattice constants of (Ga,Co)N and (Ga,Cr)N change due to the presence of Co and Cr, respectively, suggesting that the locations of the new peaks depend on the cobalt or chromium content in the material. The shift of additional peaks towards the high angle side with annealing points to lattice recovery and improvement in the uniformity of GaCoN or GaCrN which may be due to increase in the substitution probability of cobalt or chromium atoms, respectively.

4. Well-defined hysteresis loops were observed even at room temperature by AGM in all implanted and subsequently annealed samples at different temperatures, eliminating the possibility of paramagnetism and superparamagnetism. The analysis of hysteresis loops for the implanted samples helps us to explore the magnetic properties of the material. No lateral shift of hysteresis loops was observed, which, therefore, exclude spin glass behaviour. These findings suggest the presence of ferromagnetic ordering in our implanted samples at room temperature. The room temperature coercivity H_c measured by AGM was about 100 Oe for all implanted and subsequently annealed samples.

5. The coercivity (H_c) at 5 K measured by SQUID for Co^+ implanted at 3 × 10^{16} ions cm^{-2} and subsequently annealed GaN samples were observed up to 275 Oe and that at 5 × 10^{16} ions cm^{-2} and subsequently annealed samples were observed up to 600 Oe. For Cr^+ implanted at 3 ×10^{16} ions cm^{-2} and subsequently annealed samples, the coercivity was observed up to 175 Oe.

6. Comparing Cr^+ implanted and Co^+ implanted samples at the same amount of dose, we observe that saturation magnetization *Ms* values are almost the same in all samples at room temperature. But at 5 K, the saturation magnetization *Ms* values are almost similar only for the samples annealed at 800°C. The *Ms* value for Cr^+ implanted and subsequently

annealed sample at 900°C is 10.7 (× 10^{-5} $emug^{-1}$) while that for Co^+ implanted sample is about 4.5 (× 10^{-5} $emug^{-1}$). A higher value of *Ms* for Cr^+ implanted GaN and annealed at 900°C suggests that samples implanted with Cr^+ ions may perform better for dilute magnetic semiconductors (DMSs) compared to Co^+ implanted. Also higher values of *Ms* for implanted samples may suggest again that 900°C is a suitable annealing temperature for the activation of dopants.

7. FC and ZFC measurements by SQUID were made on Co^+ and Cr^+ implanted representative samples subsequently annealed at 900°C. The data did not indicate any blocking temperature that can be associated with superparamagnetic behaviour arising from undetected magnetic secondary phase clusters. Magnetization as a function of temperature showed the highest reported Curie temperature $T_C \sim 370$ K for Co^+ implanted GaN and highest reported T_C above the measured temperature (380 K) for Cr^+ implanted GaN. These findings are the highest reported Curie temperatures (T_C) for Co^+ and Cr^+ implanted GaN diluted magnetic semiconductors (DMSs).

Acknowledgements

Morgan Madhuku acknowledges iThemba LABS and the National Research Foundation of South Africa for financial support.

Author details

Ghulam Husnain[1,2] and Morgan Madhuku[1,2]*

*Address all correspondence to: morgan.madhuku@gmail.com

1 National Centre for Physics, Islamabad, Pakistan

2 iThemba LABS, NRF, Johannesburg, South Africa

References

[1] M.O. Manasreh, "III-nitride semiconductors: electrical, structural and defects properties". Elsevier Science, Amsterdam, Netherlands (2000).

[2] S.J. Pearton, C.R. Abernathy, G.T. Thaler, R. Frazier, F. Ren, and A.F. Hebard, "Effects of defects and doping on wide band gap ferromagnetic semiconductors." Physica B: Physics of Condensed Matter **340** 39-47 (2003).

[3] K. Kubota, Y. Kobayashi, and K. Fujimoto, "Preparation and properties of III-V nitride thin film." Journal of Applied Physics **66** 2984 (1989).

[4] S. Kucheyev, J. Williams, and S. Pearton, "Ion implantation into GaN." Materials Science & Engineering R **33** (2-3) 51-108 (2001).

[5] S.J. Pearton, C.B. Vartuli, J.C. Zolper, C. Yuan, and R.A. Stall, "Ion implantation doping and isolation of GaN." Applied Physics Letters **67** 1435 (1995).

[6] J.M.D. Coey, M. Venkatesan, and C.B. Fitzgerald, "Donor impurity band exchange in dilute ferromagnetic oxides." Nature Materials **4** (2) 173-179 (2005).

[7] G. Schmidt and L.W. Molenkamp, "Spin injection into semiconductors, physics and experiments." Semiconductor Science and Technology **17** 310-321 (2002).

[8] I. Zutic, J. Fabian, and S. Das Sarma, "Spintronics: Fundamentals and applications." Reviews of Modern Physics **76** (2) 323-410 (2004).

[9] A.H. MacDonald, P. Schiffr, and N. Samarth, "Ferromagnetic semiconductors: moving beyond (Ga, Mn) As." Nature Materials **4**, 195-202 (2005).

[10] J.K. Furdyna, "Diluted magnetic semiconductors." Journal Applied Physics **64** R29 (1988).

[11] S.J. Pearton, C.R. Abernathy, G.T. Thaler, R.M. Frazier, D.P. Norton, F. Ren, Y.D. Park, J.M. Zavada, I.A. Buyanova, and W.M. Chen, "Wide bandgap GaN-based semiconductors for spintronics." Journal of Physics Condensed Matter **16** (7) 209-245 (2004).

[12] T. Dietl, H. Ohno, F. Matsukura, J. Cibert, and D. Ferrand, "Zener model description of ferromagnetism in zinc-blende magnetic semiconductors." Science **287** (5455) 1019 (2000).

[13] M.L. Reed, N.A. El-Masry, H.H. Stadelmaier, M.K. Ritums, M.J. Reed, C.A. Parker, J.C. Roberts, and S.M. Bedair, "Room temperature ferromagnetic properties of (Ga, Mn) N." Applied Physics Letters **79** 3473 (2001).

[14] G. Thaler, M. Overberg, B. Gila, R. Frazier, C. Abernathy, S. Pearton, J. Lee, S. Lee, Y. Park, and Z. Khim, "Magnetic properties of n-GaMnN thin films." Applied Physics Letters **80** 3964 (2002).

[15] S. Sonoda, S. Shimizu, T. Sasaki, Y. Yamamoto, and H. Hori, "Molecular beam epitaxy of wurtzite (Ga,Mn)N films on sapphire (0001) showing the ferromagnetic behaviour at room temperature." Journal of Crystal Growth **237-239** 1358-1362 (2002).

[16] K. Sato and H. Katayama-Yoshida, "Material design of GaN-based ferromagnetic diluted magnetic semiconductors." Japanese Journal of Applied Physics **Part 2, 40** (5B) L485-487 (2001).

[17] Y. Matsumoto, M. Murakami, T. Shono, T. Hasegawa, T. Fukumura, M. Kawasaki, P. Ahmet, T. Chikyow, S. Koshihara, and H. Koinuma, "Room-temperature ferromagnetism in transparent transition metal-doped titanium dioxide." Science **291** (5505) 854 (2001).

[18] K. Ueda, H. Tabata, and T. Kawai, "Magnetic and electric properties of transition-metal-doped ZnO films." Applied Physics Letters **79** 988 (2001).

[19] A. Hebard, R. Rairigh, J. Kelly, S. Pearton, C. Abernathy, S. Chu, and R. Wilson, "Mining for high Tc ferromagnetism in ion-implanted dilute magnetic semiconductors." Journal of Physics D, Applied Physics **37** (4) 511-517 (2004).

[20] J. Lee, J. Lim, Z. Khim, Y. Park, S. Pearton, and S. Chu, "Magnetic and structural properties of Co, Cr, V ion-implanted GaN." Journal of Applied Physics **93** 4512 (2003).

[21] A. Polyakov, N. Smirnov, A. Govorkov, N. Pashkova, J. Kim, F. Ren, M. Overberg, G. Thaler, C. Abernathy, and S. Pearton, "Electrical and optical properties of GaN films implanted with Mn and Co." Journal of Applied Physics **92** 3130 (2002).

[22] D. Norton, M. Overberg, S. Pearton, K. Pruessner, J. Budai, L. Boatner, M. Chisholm, J. Lee, Z. Khim, and Y. Park, "Ferromagnetism in cobalt-implanted ZnO." Applied Physics Letters **83** 5488 (2003).

[23] L. Xue-Chao, S. Er-Wei, C. Zhi-Zhan, Z. Hua-Wei, Z. Tao, and S. Li-Xin, "Difference in magnetic properties between Co-doped ZnO powder and thin film." Chinese Physics **16** 1770-1775 (2007).

[24] S. Von Molnar and D. Read, "Magneto-transport in magnetic compound semiconductors and metals." Journal of Magnetism and Magnetic Materials **242** 13-20 (2002).

[25] S. Pearton, C. Abernathy, M. Overberg, G. Thaler, D. Norton, N. Theodoropoulou, A. Hebard, Y. Park, F. Ren, and J. Kim, "Wide band gap ferromagnetic semiconductors and oxides." Journal of Applied Physics **93** 1 (2003).

[26] S. Pearton, C. Abernathy, D. Norton, A. Hebard, Y. Park, L. Boatner, and J. Budai, "Advances in wide bandgap materials for semiconductor spintronics." Materials Science and Engineering: R: Reports **40** (4) 137-168 (2003).

[27] A. Polyakov, N. Smirnov, A. Govorkov, and S. Pearton, "Electrical and optical properties of Fe-doped semi-insulating GaN templates." Applied Physics Letters **83** 3314 (2003).

[28] R. Vaudo, X. Xu, A. Salant, J. Malcarne, and G. Brandes, "Characteristics of semi-insulating, Fe-doped GaN substrates." Physica Status Solidi(a) **200** (1) 18-21 (2003).

[29] S. Heikman, S. Keller, S. DenBaars, and U. Mishra, "Growth of Fe doped semi-insulating GaN by metalorganic chemical vapor deposition." Applied Physics Letters **81** 439 (2002).

[30] R. Korotkov, J. Gregie, and B. Wessels, "Optical properties of the deep Mn acceptor in GaN: Mn." Applied Physics Letters **80** 1731 (2002).

[31] T. Graf, M. Gjukic, M. Brandt, M. Stutzmann, and O. Ambacher, "The Mn acceptor level in group III nitrides." Applied Physics Letters **81** 5159 (2002).

[32] A. Polyakov, A. Govorkov, N. Smirnov, N. Pashkova, G. Thaler, M. Overberg, R. Frazier, C. Abernathy, S. Pearton, and J. Kim, "Optical and electrical properties of GaMnN films grown by molecular-beam epitaxy." Journal of Applied Physics **92** 4989 (2002).

[33] A. Polyakov, N. Smirnov, A. Govorkov, N. Pashkova, A. Shlensky, S. Pearton, M. Overberg, C. Abernathy, J. Zavada, and R. Wilson, "Electrical and optical properties of Cr and Fe implanted n-GaN." Journal of Applied Physics **93** 5388 (2003).

[34] A. Polyakov, N. Smirnov, A. Govorkov, S. Pearton, and J. Zavada, "Electrical and optical properties of p-GaN films implanted with transition metal impurities." Journal of Physics: Condensed Matter **16** 2967 (2004).

[35] M. Hashimoto, Y. Zhou, M. Kanamura, and H. Asahi, "High temperature (>400 K) ferromagnetism in III-V-based diluted magnetic semiconductor GaCrN grown by ECR molecular-beam epitaxy." Solid State Communications **122** (1-2) 37-39 (2002).

[36] S. Pearton, C. Abernathy, G. Thaler, R. Frazier, F. Ren, A. Hebard, Y. Park, D. Norton, W. Tang, and M. Stavola, "Effects of defects and doping on wide band gap ferromagnetic semiconductors." Physica B: Physics of Condensed Matter **340** 39-47 (2003).

[37] JF Ziegler, JP Biersack, and U. Littark, "The Stopping and Range of Ions in Matter." Pergamon Press, New York (1985). http://www.srim.org/

[38] J. Lindhard, M. Scharff and H. Schiott "Range Concepts and Heavy Ion Ranges (Notes On Atomic Collisions, II) Mat." Fys. Medd. Dan. Vid. Selsk, 1-42 (1963).

[39] S. Rubin, T. Passell, and L. Bailey, "Chemical analysis of surfaces by nuclear methods." Analytical Chemistry **29** (5) 736-743 (1957).

[40] J. Tesmer, M. Nastasi, J. Barbour, C. Maggiore, and J. Mayer, "Handbook of Modern Ion Beam Materials Analysis." Materials Research Society, Pittburgh, PA (1995), pp. 40.

[41] G. Amsel, "CUTBA (Cleaning Up the Tower of Babel of Acronyms) in IBA." Nuclear Instruments and Methods in Phys Res-Section B Only-Beam Interact Mater Atoms **118** (1) 52-56 (1996).

[42] R. L. Fagaly, "Superconducting quantum interference device instruments and applications". Review of Scientific Instruments, 77, 101101 (2006).

[43] G. Kioseoglou, A.T. Hanbicki, and B. Jonker, "Comment on "Ferromagnetism in Cr-doped Ge" [Appl. Phys. Lett. 81, 3606 (2002)]." Applied Physics Letters **83** 2716-2717 (2003).

[44] B. Warren, "X-Ray Diffaction". Dover Publications, New York, USA (1990), pp. 99.

[45] C. Liu, B. Mensching, K. Volz, and B. Rauschenbach, "Lattice expansion of Ca and Ar ion implanted GaN." Applied Physics Letters **71** (16) 2313-2315 (1997).

[46] B. Pong, C. Pan, Y. Teng, G. Chi, W. Li, K. Lee, and C. Lee, "Structural defects and microstrain in GaN induced by Mg ion implantation." Journal of Applied Physics **83** 5992 (1998).

[47] F-R. Ding, W-H. He, A. Vantomme, B.P. Q. Zhao, K. Jacobs, and I. Moerman, "Lattice expansion induced by Zn channeled implantation in GaN." Materials Science in Semiconductor Processing **5** (6) 511-514 (2002).

[48] S. Qadri, B. Molnar, M. Yousuf, and C. Carosella, "X-ray determination of strain in ion implanted GaN." Nuclear Instruments and Methods in Physics Research, B **190** (1-4) 878-881 (2002).

[49] F. Zhang, N. Chen, X. Liu, Z. Liu, S. Yang, and C. Chai, "The magnetic and structure properties of room-temperature ferromagnetic semiconductor (Ga, Mn) N." Journal of Crystal Growth **262** (1-4) 287-289 (2004).

[50] A. Luukkainen, J. Keinonen, and M. Erola, "Density and size of neon bubbles in molybdenum, tantalum, and tantalum oxide." Physical Review B **32** (7) 4814-4817 (1985).

[51] V. Vishnyakov, S. Donnelly, and G. Carter, "The influence of impurities on the growth of helium-induced cavities in silicon." Journal of Applied Physics **94** 238 (2003).

[52] D. Follstaedt, S. Myers, J. Barbour, G. Petersen, J. Reno, L. Dawson, and S. Lee, "Formation of cavities in GaAs and InGaAs." Nuclear Instruments and Methods in Physics Research, B **160** (4) 476-498 (2000).

[53] E. Oliviero, M. David, M. Beaufort, J. Nomgaudyte, L. Pranevicius, A. Declemy, and J. Barbot, "Formation of bubbles by high dose He implantation in 4H–SiC." Journal of Applied Physics **91** 1179 (2002).

[54] M. Chicoin, S. Roorda, R.A. Masut, and P. Desjardins, "Nanocavities in He implanted InP." Journal of Applied Physics **94** (9) 6116-6121 (2003).

[55] G. Ouyang, X. Tan, M. Cai, and G. Yang, "Surface energy and shrinkage of a nanocavity." Applied Physics Letters **89** 183104 (2006).

[56] V. Joshkin, C. Parker, S. Bedair, L. Krasnobaev, J. Cuomo, R. Davis, and A. Suvkhanov, "Fine structure of near-band-edge photoluminescence in He-irradiated GaN grown on SiC." Applied Physics Letters **72** 2838 (1998).

[57] D. Alquier, C. Bongiorno, F. Roccaforte, and V. Raineri, "Interaction between dislocations and He-implantation-induced voids in GaN epitaxial layers." Applied Physics Letters **86** 211911 (2005).

[58] Y. Cui and L. Li, "Suppression of phase segregation during molecular-beam epitaxial growth of GaMnN using nitrogen–hydrogen plasma." Applied Physics Letters **80** 4139 (2002).

[59] Y. Shi, Y. Zhang, C. Jiang, D. Fu, and X. Fan, "The influence of implantation temperature on the magnetism and structure of Mn^+ implanted p-GaN films." Physica B: Physics of Condensed Matter **388** (1-2) 82-86 (2007).

[60] M.F. Wu, C.C. Chen, D. Zhu, S. Zhou, A. Vantomme, G. Langouche, B.S. Zhang, and H. Yang, "Depth Dependence of the tetragonal distortion of a GaN layer on Si (111) studied by Rutherford backscattering/channeling." Applied Physics Letters **80** 4130 (2002).

[61] D. Zhi-Bo, W. Wei, W. Kun, F. Tao, and S.D. Yao, "Tetragonal distortion of InN thin films by RBS/channeling." Chinese Physics Letters **26** 086111 (2009).

[62] L.R. Doolittle, "Algorithms for the Rapid simulation of Rutherford backscattering spectra." Nuclear Instruments and Methods in Physics Research Section B: Beam Interactions with Materials and Atoms **9** (3) 344-351 (1985).

[63] A. Majid, R. Sharif, G. Husnain, and A. Ali, "Annealing effects on the structural, optical and magnetic properties of Mn implanted GaN." Journal of Physics D: Applied Physics **42** 135401 (2009).

[64] L.M. Xu, Y.P. Yu, X.J. Xing, X.Y. Wu, and S.W. Li, "Enhancement of ferromagnetism upon thermal annealing in plasma assisted MBE grown mixed-phase Mn-doped insulating TiO_2 thin films." Applied Physics A: Materials Science & Processing **92** (2) 361-365 (2008).

[65] J. Hwang, Y. Ishida, M. Kobayashi, H. Hirata, K. Takubo, T. Mizokawa, A. Fujimori, J. Okamoto, K. Mamiya, and Y. Saito, "High-energy spectroscopic study of the III-V nitride-based diluted magnetic semiconductor $Ga_{1-x}Mn_xN$." Physical Review B **72** (8) 85216 (2005).

[66] G. Husnain, F. Tao, Y. Shu-De, "Structural and magnetic properties of Co^+ implanted n-GaN dilute magnetic semiconductors." Physica B **405** 2340-2343 (2010).

[67] G. Husnain, Yao Shu-De, Ishaq Ahmad, H. M. Rafique and Arshad Mahmood "Characterization of n-GaN dilute magnetic semiconductors by cobalt ions implantation at high-fluence." Journal of Magnetism and Magnetic Material, **324** 797-801 (2012).

[68] G. Husnain, Yao Shu-De, Ishaq Ahmad and H.M. Rafique "Structural and magnetic impact of Cr^+-implantation into GaN thin film." Solid State Sciences **14,** 735-738 (2012).